Synthesis, Characterization, and Variable Range Hopping Transport of Pyrite (FeS_2) Nanorods, Nanobelts, and Nanoplates

Miguel Cabán-Acevedo, Dong Liang, Kit S. Chew, John P. DeGrave, Nicholas S. Kaiser, and Song Jin*

Department of Chemistry, University of Wisconsin—Madison, 1101 University Avenue, Madison, Wisconsin 53706, United States

ABSTRACT We report the growth, structural, and electrical characterization of single-crystalline iron pyrite (FeS_2) nanorods, nanobelts, and nanoplates synthesized *via* sulfidation reaction with iron dichloride ($FeCl_2$) and iron dibromide ($FeBr_2$). The as-synthesized products were confirmed to be single-crystal phase pure cubic iron pyrite using powder X-ray diffraction, Raman spectroscopy, and transmission electron microscopy. An intermediate reaction temperature of 425 °C or a high sulfur vapor pressure under high temperatures was found to be critical for the formation of phase pure pyrite. Field effect transport measurements showed that these pyrite nanostructures appear to behave as a moderately p-doped semiconductor with an average resistivity of $2.19 \pm 1.21\ \Omega \cdot$ cm, an improved hole mobility of 0.2 $cm^2\ V^{-1}\ s^{-1}$, and a lower carrier concentration on the order of 10^{18}—10^{19} cm^{-3} compared with previous reported pyrite nanowires. Temperature-dependent electrical transport measurements reveal Mott variable range hopping transport in the temperature range 40—220 K and transport *via* thermal activation of carriers with an activation energy of 100 meV above room temperature (300—400 K). Most importantly, the transport properties of the pyrite nanodevices do not change if highly pure (99.999%) precursors are utilized, suggesting that the electrical transport is dominated by intrinsic defects in pyrite. These single-crystal pyrite nanostructures are nice platforms to further study the carrier conduction mechanisms, semiconductor defect physics, and surface properties in depth, toward improving the physical properties of pyrite for efficient solar energy conversion.

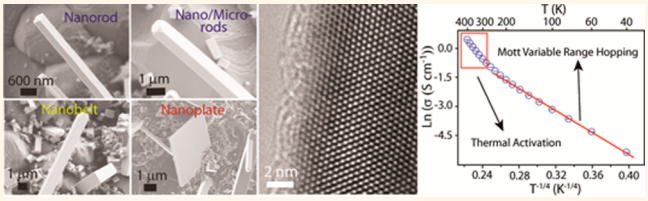

KEYWORDS: iron pyrite · nanostructure · solar energy conversion · semiconductor transport · photovoltaics · photoelectrochemistry

Iron pyrite (cubic FeS_2), commonly known as "fool's gold", is an inexpensive and earth-abundant semiconductor material with the potential to satisfy the annual worldwide energy demand.[1,2] Its indirect band gap of 0.95 eV and high absorption coefficient of $\alpha = 6 \times 10^5\ cm^{-1}$ (for $h\nu > 1.3$ eV)[1,3] make pyrite an attractive thin-layer absorber for photovoltaic and photoelectrochemical applications. Single-crystal n-type pyrite has been reported to have a high electron carrier mobility of 360 $cm^2\ V^{-1}\ s^{-1}$ and an estimated minority carrier diffusion length of 0.1—1 μm.[4] In liquid junction photoelectrochemical (PEC) solar cells, n-type single-crystal pyrite has demonstrated photocurrents as high as 42 mA cm^{-2} and an excellent stability attributed to carrier excitation occurring only within nonbonding orbitals (from the metal d_{t2g} to d_{eg}).[5] Despite its attractive properties, the best solar conversion efficiency reported for any pyrite-based solar devices has remained below 3%, which was achieved with a single-crystal pyrite PEC solar cell.[1,6] Such low efficiencies are the result of the low open circuit voltage (≤200 mV) and low fill factor (~50%) attributed mainly to high recombination losses and Fermi level pinning arising from a high density of surface defects states.[5—8] Additionally, bulk defects, believed to originate from sulfur vacancies, contribute to more severe recombination losses even in single crystals.[9,10] Except for the successful solar devices using high-quality pyrite single crystals reported in the late 1980s and early 1990s,[1,5,6] working solar devices based on nanostructure or polycrystalline pyrite thin films with detectable photovoltage have not yet been demonstrated despite intense efforts. Pyrite thin films have been grown using a variety of methods such as metal—organic chemical vapor deposition,[11,12] atmospheric pressure chemical vapor deposition,[13]

* Address correspondence to jin@chem.wisc.edu.

Received for review December 17, 2012 and accepted January 20, 2013.

Published online January 21, 2013
10.1021/nn305833u

thermal sulfidation of iron,[14−16] and sulfidation of Fe_2O_3 (hematite).[17,18] Moreover, recent renewed efforts have aggressively targeted the colloidal synthesis of pyrite nanocrystals as a cost-effective alternative to fabricating thin films.[19−22] Regardless of the synthetic methods, nanocrystalline and polycrystalline pyrite materials appear to consistently exhibit high concentrations of holes as majority carriers (and likely low carrier mobilities) and a lack of photovoltage and thus photoconversion efficiencies.[18,20,23,24] Clearly the seemingly simple pyrite material is a very complex semiconductor that needs to be better understood, and evidence suggests that it is riddled with various intrinsic defects. Acquiring high-quality crystalline pyrite and a comprehensive understanding of the defects and how they limit the semiconductor properties and solar performance will be essential for the development of pyrite as an efficient solar material.

Single-crystal one-dimensional (1D) pyrite nanowires (NWs) were recently proposed as an attractive platform to study the properties of pyrite relevant to solar energy conversion[25] and to further investigate important material challenges such as surface state passivation. Successful studies of nanowires (or microwires) made of conventional semiconductors such as Si,[26−33] CdTe,[34] and CdS/Cu_2S[35] for solar devices suggest that 1D pyrite nanostructures could have various unique properties of the 1D morphology over planar geometries for solar applications.[32,36] These examples also clearly illustrate that high-quality nanoscale 1D building blocks can allow the fundamental investigation of intrinsic semiconductor properties, surface and interfaces, and heterojunction formation to overcome the bottlenecks for solar energy conversion.[27] Despite these potential advantages, the growth of single-crystalline 1D pyrite nanostructures that are convenient for electrical device investigations remains relatively unexplored.[25]

Herein, we report a synthetic approach for single-crystal and phase pure pyrite nanorods (NRs), nanobelts (NBs), and nanoplates *via* thermal sulfidation reactions with iron dichloride ($FeCl_2$) and iron dibromide ($FeBr_2$) and a detailed characterization of structures and electrical transport properties. The phase purity of the reported pyrite nanostructures is confirmed using various structural characterization methods. Furthermore, the size and geometry of these single-crystal pyrite nanostructures enable the investigation of the properties and intrinsic defects of pyrite semiconductor. The field-effect semiconductor transport measurements show that the as-synthesized pyrite behaves analogously to a moderately doped p-type semiconductor, but with higher mobilities than previous reported pyrite nanostructures. More importantly, temperature-dependent electrical measurements revealed the carrier transport in pyrite to be dominated by localized defect states *via* the Mott variable range hopping mechanism at low temperature.

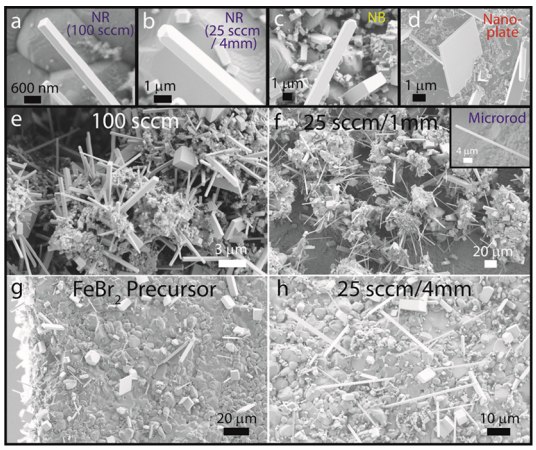

Figure 1. Representative SEM images of as-synthesized iron pyrite nanostructures grown at a reactor temperature of 425 °C. Representative examples of (a, b) NR, (c) NB, and (d) nanoplate and overview images (e−h): (e) pyrite NRs obtained using $FeCl_2$ as precursor under an argon flow rate of 100 sccm; (f) pyrite microrod product obtained under a lower flow rate of 25 sccm on a 1 mm thick borosilicate substrate; (g) pyrite NBs and nanoplates are the predominant morphologies on the alumina substrate surface when $FeBr_2$ is used as the precursor; (h) when $FeCl_2$ precursor is evenly spread on a 4 mm thick alumina substrate, pyrite NR growth is observed on its surface.

RESULTS AND DISCUSSION

Synthesis of Pyrite (FeS_2) NRs, NBs, and Nanoplates. We achieved the synthesis of iron pyrite NRs, NBs, and nanoplates (Figure 1a−d) by heating dehydrated $FeCl_2$ or $FeBr_2$ precursor powder at 425 °C under a flowing sulfur atmosphere. Sulfur powder was evaporated upstream from an alumina boat, carried downstream by an argon flow, and reacted with the $FeCl_2$ or $FeBr_2$ precursor on an alumina or borosilicate substrate in the hot zone of the tube furnace. Square-faceted NRs (Figure 1a) were obtained as the predominant product on the substrates when $FeCl_2$ was utilized as the precursor and the sulfur boat was at a temperature of 415 °C, yielding an equilibrium S_x vapor pressure of ~300 Torr, and under an Ar flow rate of 100 sccm. A representative overview SEM image of the as-synthesized product (Figure 1e) shows that NR growth took place at the surface of the precursor grains. However, the high Ar flow rate employed led to a fast depletion of sulfur precursor and an incomplete reaction of the $FeCl_2$ precursor. As an alternative, we studied the low Ar flow rate regime and observed optimal growth at a Ar flow rate of 25 sccm and with the sulfur boat at a temperature of 240 °C, which yields ~8 Torr equilibrium S_x vapor pressure. Under this reaction conditions, an interesting dependence of the product morphology on the substrate height was observed. For example, on 1 mm thick alumina or borosilicate substrates, microrod growth was observed on the precursor powder (Figure 1f). On the other hand, when 4 mm thick substrates were utilized, NR, NB, and microrod growth were observed on the substrate surface underneath

the precursor powder (Figure 1h). Consequently, in order to obtain growth across the 4 mm thick substrate, the precursor powder was evenly spread onto the substrates and subsequently removed after reaction by blowing a stream of N_2 gas and gentle rinsing with 2-propanol. Unless otherwise noted, the pyrite NRs and NBs from this particular $FeCl_2$ reaction were the focus of the structural characterization and electrical transport measurements discussed later.

Pyrite NRs, NBs, and nanoplates can also be grown through a localized gas phase reaction when $FeBr_2$ is utilized as the iron precursor. When the $FeBr_2$ precursor was located at the center of a substrate, deposition of pyrite NBs, nanoplates, and NRs on the uncovered areas of the substrate could be observed (Figure 1g) at a sulfur boat temperature of 400 °C (~270 Torr equilibrium S_x vapor pressure) and an Ar flow rate of 50 sccm. Under this reaction condition the NB and nanoplate morphologies were more predominant than in the $FeCl_2$ reaction. When the sulfur vapor pressure was lowered, little deposition elsewhere was observed, although cubic pyrite crystals were grown on the surface of the precursor. When the Ar flow rate was increased, an enhancement in NR and NB growth was observed, but the fast depletion of the sulfur affected the crystallinity of the products.

Through systematic studies of the sulfur boat temperature, Ar flow rate, and different reactor temperatures we found that the intermediate reaction temperature of 425 °C and suitable sulfur supersaturation, especially a high sulfur vapor pressure under high temperature (as discussed more later), are important for the formation of pyrite nanostructures. The growth of pyrite NRs and NBs is influenced by the local sulfur supersaturation, which is controlled by the sulfur precursor boat temperature (position) and Ar flow rate. The Ar flow rate when the sulfur boat is at high temperature or the sulfur boat position under low Ar flow rates causes more dramatic changes. It is important to note that under low flow rate mass transport of gaseous species is affected more by thermal diffusion rather than conventional flow. Thermal diffusion transport leads to a concentration gradient within the reactor that could explain the substrate height dependency observed (Figure 1f, h). Extensive research has shown that growth of catalyst-free 1D structures can occur under low supersaturation conditions due to the dominant defect-driven anisotropic crystal growth.[37−40] The conditions needed for generating defective seeds to initiate 1D growth could also allow other crystal growth modes,[38−40] evident in our experiment by the nanoplate, nanocube, and microcube morphologies also observed. However, the variations in morphology are not an issue for using these nanostructures as platforms and building blocks for fundamental studies as demonstrated later in this work.

Structural Characterization of the Pyrite Nanostructures. The phase identity of the as-synthesized products on

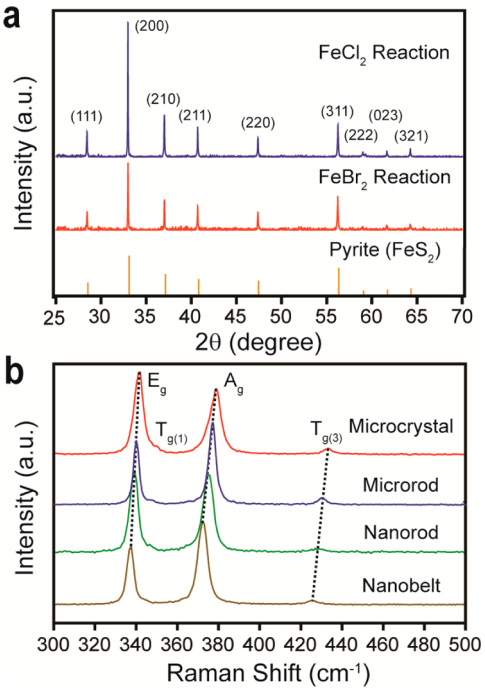

Figure 2. Structural characterization of the as-synthesized pyrite products. (a) PXRD taken on as-synthesized products made from $FeCl_2$ and $FeBr_2$ precursors on borosilicate substrates, in comparison to the reference diffraction pattern for pyrite (JCPDS #65-3321). (b) Confocal micro-Raman spectroscopy for different pyrite morphologies on borosilicate substrates using a 532 nm laser.

borosilicate substrate using both $FeCl_2$ and $FeBr_2$ precursors was determined using powder X-ray diffraction (PXRD) (Figure 2a). All peaks in the PXRD can be indexed exclusively to iron pyrite (cubic FeS_2, JCPDS #65-3321; space group $Pa\bar{3}$, a = 5.419 Å). It should be noted that it is important to calculate the lattice constant from the PXRD, because it has been previously reported that the lattice constant of synthetic pyrite can vary from 5.428 to 5.407 Å, which is attributed to sulfur vacancies in pyrite (up to 13%, $FeS_{1.74}$) grown at high sulfidation temperatures (≥450 °C) or prolonged annealing times, causing up to 1% lattice compression.[41,42] The average lattice constant of the as-synthesized pyrite products herein was found to be 5.424 Å, in agreement with stoichiometric pyrite.

Furthermore, we used confocal micro-Raman spectroscopy to confirm the phase purity of individual pyrite objects with different morphologies. Raman spectroscopy has been found to be a more sensitive technique to differentiate the marcasite FeS_2 impurity in pyrite samples and effectively used to ascertain phase purity.[13,25] The Raman spectrum for a microcrystal (Figure 3b top trace) shows three peaks, at 342, 379, and 433 cm^{-1}. These peaks are the characteristic active modes for bulk pyrite corresponding to the S_2 libration (E_g), S−S in-phase stretch (A_g), and coupled libration and stretch (triply degenerate, specifically $T_{g(3)}$) modes, respectively.[43,44] Additionally, the weak $T_{g(1)}$ mode can

be observed as a small shoulder peak at 350 cm^{-1}. No peaks corresponding to the marcasite polymorph are observed. Interestingly, even though the Raman peaks for other structures still generally match those of pyrite, a systematic red-shift of these peaks is observed for the microrod, NR, and NB morphologies. For example, an observed NB shows values of 338, 373, and 427 cm^{-1}, respectively. We attribute the observed red-shift to sample heating due to laser irradiation, since a shift to higher energies and oxidation of the nanostructures were observed when the laser intensity was not attenuated. Additionally we found that this red-shift becomes more pronounced as the dimensions of the probed nanostructures become smaller (Figure 2b). Interestingly, a more evident peak shift for the A_g mode in comparison to the E_g mode is observed. The A_g phonon mode involves purely the vibration of the S_2 dumbbell; consequently, faster softening of this phonon mode perhaps reflects the weaker bond strength for S−S in comparison to Fe−S.

The single-crystal phase of the pyrite NRs and NBs was further confirmed by transmission electron microscopy (TEM), electron diffraction (ED), and fast Fourier transform (FFT) analysis. Representative TEM images (Figure 3a, c) of single-crystal NRs oriented along the [100] and [110] zone axes (ZAs) were indexed to cubic iron pyrite (space group $Pa\bar{3}$, a = 5.419 Å) using their corresponding ED patterns (Figure 3b, d). Further evidence of the single-crystal iron pyrite phase was obtained from HRTEM (Figure 3e) by indexing the corresponding FFT to the [111] ZA pattern. The observation of the [110] and [111] ZA patterns provides convincing evidence to differentiate cubic pyrite from its orthorhombic polymorph marcasite, as we previously demonstrated for pyrite nanowires.[25] Note some double diffraction spots were observed due to the rather large thickness of these pyrite nanostructures. All pyrite NRs and NBs analyzed exhibited the same ⟨001⟩ axial growth direction (Figure 3e) based on indexed ED patterns and high-resolution images. These square-faceted NRs, NBs, and nanoplates offer the unique advantage of having only the {100} exposed facets, which is the most stable surface for pyrite.[45−47]

Interestingly, planar defects were often observed along the axial length of NR and NB (Figure 3f) when viewed along the ⟨010⟩ ZA. The observed planar defects, which are not always at the center, were identified using HRTEM images as stacking faults in a single faulted region or as multiple faults (Figure 3g, h). Axial stacking faults have been observed in pyrite crystals and NWs along a [100] pyrite projection, and the displacement vector has been characterized to be **R** = 0.115[001].[25,48] Notably, no dangling bonds are to be expected in such stacking faults; instead the arrangement of atoms due to the displacement vector results in a unit cell that resembles marcasite (monolayer or lamella marcasite). A previous report suggests that such stacking fault defects are not expected to be detrimental for photovoltaics or to induce deep energy levels in various materials.[49]

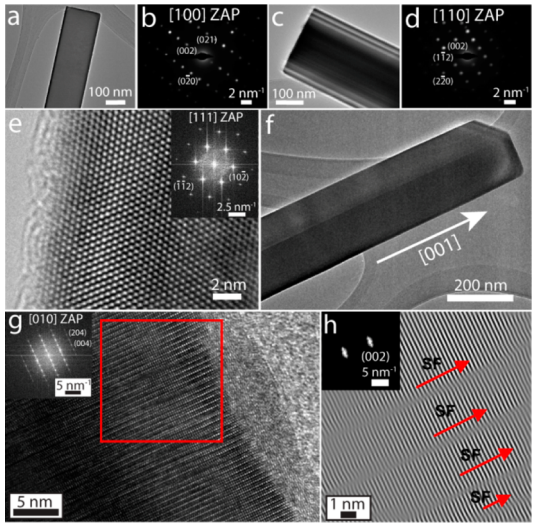

Figure 3. TEM characterization of pyrite NRs and NBs. (a−d) TEM and the corresponding electron diffraction patterns for a pyrite NB oriented along the [100] (a, b) and a NR along the [110] ZA (c, d). (e) HRTEM and the corresponding fast Fourier transform (FFT) (inset) of a pyrite NR oriented along the [111] ZA. Note some extra diffraction spots at high angle come from a nearby object. (f) TEM image of a pyrite NB displaying axial planar defect contrast. (g) HRTEM image and the corresponding FFT of the tip of a single NR along the [010] ZA. (h) Image from selected area in (g) after Fourier filtered using the (002) diffraction spots highlighting the axial stacking faults.

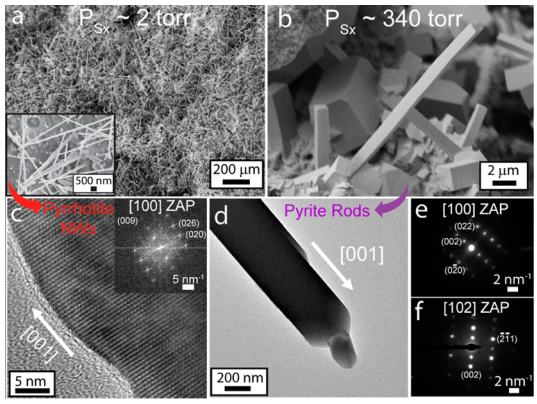

Figure 4. SEM images of the iron sulfide products at a reaction temperature of 500 °C. (a) SEM image of the pyrrhotite NW product obtained when the sulfur boat was at a temperature of 200 °C (which yields ~2 Torr equilibrium S_x vapor pressure); (b) pyrite rod product obtained when the sulfur boat was at a temperature of 415 °C (which yields 340 Torr equilibrium S_x vapor pressure); (c) HRTEM image and the corresponding FFT along the [100] ZA of pyrrhotite, for a representative NW from (a); (d) TEM image and the corresponding EDs along the [100] and [102] ZA of pyrite, for a representative rod from (b).

Thermal Stability and Formation Window of Iron Pyrite. We also investigated the reactions at the high reaction temperature regime of 500−600 °C in an attempt to enhance the vapor pressure of the $FeCl_2$ and $FeBr_2$

precursors. We found that as the reaction temperature increases, the sulfur vapor pressure required to obtain phase pure iron pyrite increases. For example, when the reaction was carried out at 500 °C and under a low sulfur vapor pressure of ~2 Torr (based on the equilibrium S_x vapor pressure for a sulfur boat temperature of 200 °C), pyrrhotite NWs were produced (Figure 4a). As shown in Figure 4c, the crystal phase of these NWs was determine using HRTEM and FFT to be trigonal Fe_7S_8 (or ~$Fe_{0.877}S$, space group $P3_121$, a = 6.966 Å, c = 17.088 Å), one of the pyrrhotite phases ($Fe_{1-x}S$) that have a defective nickel arsenide structure type. This phase identification is consistent with a previous report of trigonal Fe_7S_8 NWs that have been synthesized under similar growth conditions.[50] On the other hand, at a high sulfur vapor pressure of ~340 Torr (sulfur boat at a temperature of 415 °C), square-faceted microcrystals, microrods, and a few NRs can be observed at the precursor source (Figure 4b). The ED pattern of a NR from this reaction was indexed to the [100] ZA and by tilting the same structure to the [102] ZA of pyrite (Figure 4d−f), as an example of the phase identification. However, in addition to the observed pyrite products we also observed pyrrhotite nanostructures as a deposition product elsewhere on the substrate.

This dependency on sulfur vapor pressure at higher temperature is not unexpected because pyrite is known to decompose to pyrrhotite based on thermodynamics data (see Supporting Information) and experimental observation using thermogravimetrical analysis.[51] The formation of iron pyrite from $FeBr_2$ (as the example) and its decomposition to pyrrhotite (using the specific Fe_7S_8 phase as an example) proceed through the following reactions:

$$FeBr_2(g) + S_2(g) = FeS_2(s) + Br_2(g) \quad (1)$$

$$7/8\ FeS_2(s) = 1/8\ Fe_7S_8(s) + 3/8\ S_2(g) \quad (2)$$

The standard Gibbs free energy (ΔG_f) for the formation of iron pyrite (eq 1) is estimated to increase from −43.3 kJ/mol at 425 °C to −24 kJ/mol at 500 °C (see Supporting Information for details). In comparison, the decomposition to pyrrhotite (eq 2) is predicted to be spontaneous at $T \geq$ 620 °C, and the standard Gibbs free energy for this reaction decreases from 37.3 kJ/mol at 425 °C to 20.5 kJ/mol at 500 °C. Note that these standard Gibbs free energy values are for the standard conditions with the gaseous species at 1 bar pressure, which is not the case for our reactions. But these estimates predict the trends, and furthermore, the decomposition in eq 2 will be even more favorable because of the gaseous sulfur product with lower pressure. Therefore, as a guideline high temperature (>425 °C) is not conducive to the formation of pure pyrite due to its decomposition, and high sulfur vapor pressure plays an important role in suppressing decomposition and stabilizing the formation of iron pyrite.

Field Effect Measurements of Single NR and NB Devices. We characterized the semiconducting properties of the as-grown pyrite NRs, NBs, and nanoplates using four-probe devices that were fabricated using standard e-beam lithography techniques and e-beam deposition of Ti/Au contacts. Figure 5a shows a typical two-probe and four-probe electrical measurement of a single pyrite NR device. Linear current (I_{sd}) *versus* voltage (V_{sd}) behavior at room temperature indicates ohmic contact. Through four-probe measurement (blue solid line in Figure 5a), a resistivity (ρ) of 4.25 Ω·cm was calculated for the pyrite NR using the dimensions measured through SEM imaging (inset of Figure 5a). The measurement of 10 four-probe NR and NB devices yielded an average resistivity of 2.19 ± 1.21 Ω·cm.

We investigated the field effect of the semiconducting pyrite using field effect transistors (FETs) fabricated with single crystal pyrite NRs, NBs, and nanoplates that are gated with a solid electrolyte consisting of a mixture of polyethylene oxide (PEO) and $KClO_4$[52,53] (Figure 5b, inset) or a back gate through a 600 nm dielectric SiO_2 layer on a degenerately doped silicon substrate (Figure 5c, inset). Figure 5b shows the typical electrolyte gating effect for a single pyrite NB device. The plot of I_{sd} *versus* V_g at V_{sd} = 0.1 V yielded a negative transconductance of 0.083 μA/V, suggestive of holes as the majority carriers. The field effect mobility (μ) and carrier concentration (N) can be estimated by $\mu = g_m L^2/(V_{sd}C_g)$ and $N = 1/\rho e\mu$ (e is electron charge). Here, C_g is double layer capacitance of electrolyte surrounding gate. Taking account of all the NB facets surrounded by electrolyte, we expressed it as $C_g = \varepsilon\varepsilon_0(2d + w)\ L/\lambda_D$ (see Supporting Information for details), where ε is the dielectric constant of PEO (~10), ε_0 is the vacuum permittivity, $\lambda_D \approx 1$ nm[54] is the Debye length of the electrolyte, d = 320 nm is the thickness, w = 1 μm is the width of the pyrite NB, and L = 2.74 μm is the NB device channel length. The gate capacitance was calculated to be $C_g = 3.98 \times 10^{-13}$ F, yielding a mobility μ = 0.150 $cm^2\ V^{-1}\ s^{-1}$ and a carrier concentration $N = 1.3 \times 10^{19}\ cm^{-3}$ at V_{PEO} = 0 V.

The mobility and carrier concentration for this NB FET device were found to be in good agreement with the less effective back gate measurements on the same device (Figure 5c), from which μ = 0.238 $cm^2\ V^{-1}\ s^{-1}$ and $n = 6.1 \times 10^{18}\ cm^{-3}$ can be calculated. Hence, through electrolyte gating FET measurements of at least 10 single NR, NB, and nanoplate (see Figure S1 in the Supporting Information) FET devices and corroboration whenever possible with back gating FET, we consistently obtained mobility close to 0.1−0.2 $cm^2\ V^{-1}\ s^{-1}$ and carrier concentration on the order of 10^{18}−$10^{19}\ cm^{-3}$ for our current pyrite devices whose smallest dimensions are about several hundred nanometers. This mobility is 1 order of magnitude larger than that previously reported for pyrite NWs, and the carrier concentration is 2−3 orders of magnitude lower.[25] We also investigated the

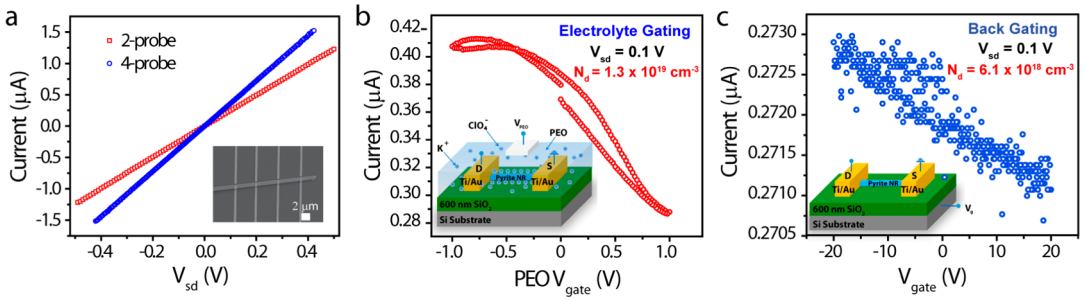

Figure 5. (a) *I*–*V* curve for a two-probe (red) and four-probe (blue) measurement of a single pyrite NR device (inset shows an SEM image of a typical device). (b) I_{sd} *versus* PEO V_g plot at V_{sd} = 0.1 V for a pyrite NB FET using an electrolyte gate configuration (inset). (c) I_{sd} *versus* V_g at V_{sd} = 0.1 V for the same pyrite NB FET using a back gate configuration (inset). This NB device is 2.74 μm long, 1.00 μm wide, and 320 nm thick.

FET behavior of pyrite NRs and NBs synthesized using high-purity $FeBr_2$ (99.999%) and sulfur powder (99.999%). Interestingly we found no significant difference in mobility or carrier concentration, strongly suggesting that dopant species originate from intrinsic defects in iron pyrite. In the case where surface defect states are responsible for the acceptor species, the observed higher carrier concentration for the previously reported thin pyrite NWs might be caused by an increase in specific surface area, considering the 2 orders of magnitude difference in diameter (or thickness) with the larger pyrite nanostructures reported herein.

Mechanisms of Electrical Transport in Pyrite Revealed by Temperature-Dependent Transport Study. We further investigated the electrical transport mechanisms in single-crystal pyrite through temperature dependence of the four-probe conductivity. The devices were fabricated with pyrite NRs, NBs, and nanoplates synthesized using high-purity precursors. Figure 6a shows the temperature dependence of conductivity for a representative NR device, plotted as ln(σ) *versus* $T^{-1/4}$. We found a linear relation in this plot in the temperature range ~40–220 K, which indicates that the conductivity as a function of temperature follows the relation predicted by the Mott variable range hopping (VRH) mechanism:[54]

$$\sigma = \sigma_0 \exp[-(T_0/T)]^{1/4} \quad (3)$$

where σ_0 is a prefactor and T_0 is the characteristic temperature, also known as the Mott VRH temperature. The exact temperature dependence of the prefactor (σ_0) is determined by the assumption made about the electron–phonon interaction during hopping.[55] It is most commonly assumed to be weakly temperature dependent; therefore as an approximation we assume that $\sigma \propto \exp[-(T_0/T)]^{1/4}$. Therefore, we plotted ln(σ) *versus* $T^{-1/4}$ in Figure 6a for a representative pyrite NR device and performed a linear fitting in the temperature range 40–220 K, from which the characteristic Mott temperature (T_0) is calculated to be 6.9 × 10^5 K. We also studied the temperature-dependent transport properties of pyrite nanoplates, which behave similarly to pyrite NRs and NB (Figure S2 in the Supporting Information). Furthermore, Mott VRH transport in the same temperature regime

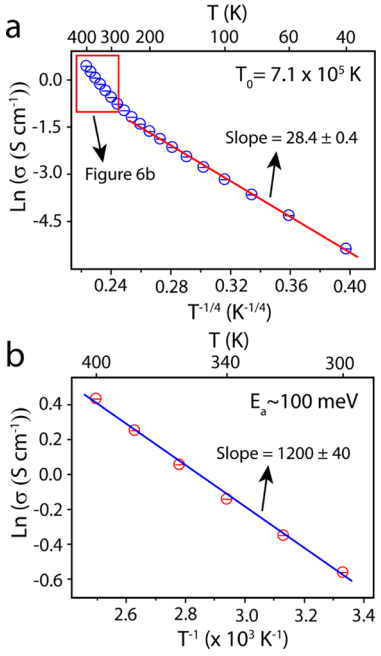

Figure 6. Conductivity (σ) of a representative pyrite NR as a function of temperature. (a) ln(σ) *versus* $T^{-1/4}$; (b) ln(σ) *versus* 1/*T* for the high-temperature range of 300–400 K. A current of 0.05 μA was applied to this 1.406 μm (L) × 511 nm (w) × 455 nm (h) NR four-probe device.

(~40–220 K) has been previously observed for pyrite polycrystalline thin films.[56,57]

Mott VRH is a conduction mechanism describing the hopping among localized states in a strongly disordered system.[55,58] In crystalline semiconductors, the disorder induced due to the random potential distribution of impurities or defect states, known as Anderson localization, is the cause of localization of charge carriers.[55,58] The upper temperature limit in which the Mott VRH transport can operate is determined by half of the Debye temperature ($T \leq \theta_D/2$), which is approximately $T \leq 300$ K for pyrite, with a reported θ_D of 610 K.[56,59] The persistence of VRH up to 220 K suggests single-crystalline pyrite is a defect-rich system. Moreover, the fact that the 3D hopping model fits for morphological 1D or 2D pyrite nanostructures (NRs, NBs, and nanoplates) suggests that the localization length is smaller than the size of pyrite nanostructures.

At temperatures higher than 220 K, a transition region was observed, followed by a change of slope in the temperature range 300−400 K. In this regime, we found the conductivity as a function of temperature follows the behavior governed by the thermal activation of carriers:[54]

$$\sigma = \sigma_1 \exp[-(\varepsilon_1/k_B T)] \quad (4)$$

where σ_1 is a temperature-independent prefactor and ε_1 corresponds to the thermal activation energy. Figure 6b shows the conductivity in the range 300−400 K for the same NR device, now plotted as ln(σ) *versus* 1/*T*. From the linear fitting the activation energy was estimated to be 100 meV, indicating a defect or impurity band located 200 meV above the valence band or below the conduction band. On the basis of the observed FET behavior, it could be localized acceptor-like states located 200 meV from the valence band. Notably both the FET measurements and the temperature-dependent transport measurements do not depend on whether high-purity (99.999%) or low-purity (98−99%) precursors ($FeCl_2$ or $FeBr_2$ and S) are used for the synthesis of the pyrite nanostructures. The Mott VRH transport can be caused by either extrinsic dopant impurities or intrinsic defects in crystalline semiconductors. However, the fact that the Mott VRH is observed for single-crystal (as opposed to polycrystalline) pyrite structures regardless of the sample purity, coupled with the FET transport behavior observed, suggests that the electrical transport is dominated by intrinsic defects in crystalline pyrite.

CONCLUSION

In conclusion, we demonstrated the first reported synthesis of single-crystalline iron pyrite nanorods, nanobelts, and nanoplate synthesized *via* a sulfidation reaction with $FeCl_2$ and $FeBr_2$. The crystalline phase of these nanostructures was confirmed to be cubic iron pyrite by TEM analysis, and the phase purity of the as-synthesized products was verified by PXRD and Raman spectroscopy. Field effect transport measurements revealed that the pyrite samples appear to behave like a moderately doped p-type semiconductor with a reduced carrier concentration and a higher mobility over previously reported pyrite NWs. Temperature-dependent transport measurements revealed that Mott variable range hopping is the dominant transport mechanism in the temperature regime ~40−220 K, while in the temperature regime of approximately 300−400 K, thermal activation of carriers with an activation energy of 100 meV was found. Most importantly, we found that the FET and temperature-dependent transport properties are independent of precursor purity. These observations suggest that the transport properties of single-crystal pyrite nanostrutures are dominated by intrinsic defects rather than extrinsic impurities. Further investigation of these single-crystal pyrite nanostructures will focus on using them as a platform to study in detail the origin of the hole conduction observed and the role of the surface and bulk defects in transport properties. Because the eventual thin film photovoltaic technology based on pyrite would likely utilize pyrite materials with a thickness of several hundred nanometers or less, these single-crystal pyrite nanostructures with similar dimensions are nice model systems for thin film device studies. We believe that a complete understanding of the defects dominating the physical properties of various pyrite materials and strategies to address them are needed in order to explain and overcome the ubiquitous heavy p-type conduction and lack of photovoltage and thus photoconversion efficiency observed throughout the literature on pyrite.

METHODS

Synthesis of Pyrite Nanorods and Nanobelts. Pyrite nanorods were synthesized in a home-built reactor consisting of a 1-in. fused silica tube placed in a single-zone tube furnace (Lindberg/Blue M) equipped with pressure and single-gas flow controls. In a typical preparation, 5 mg of $FeCl_2 \cdot 4H_2O$ (99.0%, Sigma-Aldrich) was uniformly distributed on the surface of a 1 cm × 1 cm × 4 mm (or 1 mm) thick alumina (Coors Tek Inc.) or borosilicate substrate. The substrates were then placed at the center of the furnace, and an alumina boat containing elemental sulfur powder (99.5%, Fisher Scientific) was placed outside the heating zone. The tube was evacuated to a base pressure of 10 mTorr and flushed three times with argon. The tube furnace was first heated under vacuum to 100 °C at a rate of ~7.5 °C/min, held at 100 °C for 30 min, and then heated to 150 °C at a rate of ~5 °C/min to dehydrate the $FeCl_2 \cdot 3H_2O$ precursor to yield a tan-colored powder.

After dehydration the tube was heated to 425 °C under an argon flow of 25 sccm at 760 Torr. Once the temperature was reached, the sulfur boat was pushed with the aid of a Teflon magnetic stir bar 3.5 cm inside the insulation opening of the tube furnace (where the sulfur boat was at a temperature of 240 °C) to initiate the reaction. After 2 h of reaction time, the reactor was cooled naturally to room temperature. Once the temperature reached 300 °C, the argon flow was stopped and the reactor evacuated. Any remaining precursor powder after reaction was removed from the substrate by blowing a stream of N_2 gas and gentle rinsing with 2-propanol.

Synthesis of Pyrite Nanobelts and Nanoplates. In a typical preparation, 5 mg of $FeBr_2$ powder (98%, Sigma-Aldrich) was piled on the center of a 1 cm × 1 cm × 4 mm (or 1 mm) thick alumina (Coors Tek Inc.) or borosilicate substrate. The procedures were similar to the case above except that for dehydrating the $FeBr_2$ hydrate precursor the tube furnace was first heated to 100 °C at a rate of ~7.5 °C/min, held at 100 °C for 30 min, and then heated to 200 °C at a rate of ~4 °C/min under vacuum. Then the tube was heated to 425 °C under an argon flow of 50 sccm at 760 Torr. Once the temperature was reached, the sulfur boat was moved 9 cm inside the insulation opening of the furnace (where the sulfur boat was at a temperature of 400 °C). After 45 min of reaction time, the reaction was cooled and terminated similarly to the case above.

Pyrite NRs, NBs, and nanoplates were also synthesized using high-purity anhydrous $FeBr_2$ powder (99.999%, Sigma-Aldrich) and elemental sulfur powder (99.999%, Materion) following the same reaction conditions including the dehydration procedure. These structures were used for some device measurements as noted.

Structural Characterization. The powder X-ray diffraction patterns of as-synthesized samples on borosilicate substrates were

collected on a Bruker D8 Advance Powder X-ray diffractometer using Cu Kα radiation. The background from the borosilicate substrate was subtracted from the raw data. The confocal micro-Raman spectra of an as-synthesized sample on the borosilicate substrate were collected with a Horiba Jobin Yvan LabRAM ARAMIS confocal microscope using a 100 μm aperture and a 532 nm laser source. All measurements were taken under the same laser intensity attenuation using a density filter to avoid oxidation of the pyrite nanostructure. For scanning electron microscopy (SEM) imaging, the as-synthesized samples were mounted onto metal pucks and bridged to their surface using double-sided carbon tape. Some samples were gold sputtered before imaging to improve the conductivity of the insulating substrates. All samples were imaged using a LEO Supra 55 VP field emission SEM. To prepare the specimen for TEM imaging, a TEM grid (Ted Pella, lacey carbon type-A support film, 300 mesh, copper, #01890-F) was placed on the surface of an as-grown substrate covered with pyrite nanostructures, and by gently rubbing the TEM grid on the substrate, nanostructures were "dry transferred". TEM imaging was carried out on a Philips CM200 TEM at an accelerating voltage of 200 kV. HRTEM was carried out on a FEI Titan scanning transmission electron microscope at an accelerating voltage of 200 kV or a Tecnai TF-30 TEM at an accelerating voltage of 300 kV (specifically for Figure 3e).

Single NR, NB, and Nanoplate Device Fabrication and Electrical Measurements. Pyrite NRs, NBs, and nanoplates were gently dry transferred onto degenerately doped Si (100) substrates coated with 600 nm of silicon dioxide. Electrodes were then defined using standard e-beam lithography, and ohmic contact to the NRs was made with e-beam evaporated Ti (70 nm thick) and Au film (30 nm thick). A 3 s buffer HF etching (buffered HF improved, Transene Inc.) of the sample before metal evaporation was found to be necessary to make ohmic contact. Room-temperature electrical and field effect characteristic measurements were made on a Cascade Microtech RF-1 probe station and a custom computerized transport setup. Back gating was applied through a degenerated doped silicon substrate separated by a 600 nm thick silicon dioxide dielectric layer. Solid electrolyte gating was performed using a PEO/$KClO_4$ electrolyte,[52,53] which was prepared by dissolving PEO/$KClO_4$ (7:1 in weight ratio) in methanol. To fabricate the electrolyte gated devices, this solution was drop-cast onto the substrate chip, which was later baked at 90 °C until residual moisture and methanol were removed.

Temperature-dependent measurements of the pyrite NR, NB, and nanoplate devices were carried out in a Quantum Design Physical Property Measurement System (PPMS-9T) combined with standard DC measurement setup using a Keithley 6221 as current source and a Keithley 2182A as voltmeter. All temperature-dependent conductivity measurements were taken at discrete temperatures at which thermal equilibrium was reached using a constant current of 0.05 μA through the device.

Conflict of Interest: The authors declare no competing financial interest.

Acknowledgment. The research is supported by the U.S. Department of Energy, SunShot NextGen PV II program under Award DE-EE0005330. M.C. thanks the NSF Graduate Research Fellowship for support. J.P.D. assisted with the low-temperature device measurements and is supported by an NSF grant (ECCS-1231916). S.J. also thanks the Research Corporation SciaLog Award for Solar Energy Conversion and UW−Madison Vilas Associate Award for support.

Supporting Information Available: Thermodynamics data on pyrite formation and decomposition. Details about the gate capacitance calculations and the gating effect and variable range transport of pyrite nanoplates. This material is available free of charge via the Internet at http://pubs.acs.org.

REFERENCES AND NOTES

1. Ennaoui, A.; Fiechter, S.; Pettenkofer, C.; Alonso-Vante, N.; Büker, K.; Bronold, M.; Höpfner, C.; Tributsch, H. Iron Disulfide for Solar Energy Conversion. *Sol. Energy Mater. Sol. Cells* **1993**, *29*, 289–370.
2. Wadia, C.; Alivisatos, A. P.; Kammen, D. M. Materials Availability Expands the Opportunity for Large-Scale Photovoltaics Deployment. *Environ. Sci. Technol.* **2009**, *43*, 2072–2077.
3. Ennaoui, A.; Fiechter, S.; Goslowsky, H.; Tributsch, H. Photoactive Synthetic Polycrystalline Pyrite (FeS_2). *J. Electrochem. Soc.* **1985**, *132*, 1579–1582.
4. Ennaoui, A.; Tributsch, H. Energetic Characterization of the Photoactive FeS_2 (Pyrite) Interface. *Solar Energy Mater.* **1986**, *14*, 461–474.
5. Ennaoui, A.; Fiechter, S.; Jaegermann, W.; Tributsch, H. Photoelectrochemistry of Highly Quantum Efficient Single-Crystalline *n*-FeS_2 (Pyrite). *J. Electrochem. Soc.* **1986**, *133*, 97–106.
6. Buker, K.; Alonso-Vante, N.; Tributsch, H. Photovoltaic Output Limitation of *n*-FeS_2 (pyrite) Schottky Barriers: A Temperature-Dependent Characterization. *J. Appl. Phys.* **1992**, *72*, 5721–5728.
7. Mishra, K. K.; Osseo-Asare, K. Fermi Level Pinning at Pyrite (FeS_2)/Electrolyte Junctions. *J. Electrochem. Soc.* **1992**, *139*, 749–752.
8. Nesbitt, H. W.; Scaini, M.; Höchst, H.; Bancroft, G. M.; Schaufuss, A. G.; Szargan, R. Synchrotron XPS Evidence for Fe^{2+}-S and Fe^{3+}-S Surface Species on Pyrite Fracture-Surfaces, and Their 3D Electronic States. *Am. Mineral.* **2000**, *85*, 850–857.
9. Birkholz, M.; Fiechter, S.; Hartmann, A.; Tributsch, H. Sulfur Deficiency in Iron Pyrite (FeS_{2-x}) and Its Consequences for Band-Structure Models. *Phys. Rev. B* **1991**, *43*, 11926–11936.
10. Bronold, M.; Pettenkofer, C.; Jaegermann, W. Surface Photovoltage Measurements on Pyrite (100) Cleavage Planes: Evidence for Electronic Bulk Defects. *J. Appl. Phys.* **1994**, *76*, 5800.
11. Höpfner, C.; Ellmer, K.; Ennaoui, A.; Pettenkofer, C.; Fiechter, S.; Tributsch, H. Stoichiometry-, Phase- and Orientation-Controlled Growth of Polycrystalline Pyrite (FeS_2) Thin Films by MOCVD. *J. Cryst. Growth* **1995**, *151*, 325–334.
12. Meester, B.; Reijnen, L.; Goossens, A.; Schoonman, J. Synthesis of Pyrite (FeS_2) Thin Films by Low-Pressure MOCVD. *Chem. Vap. Deposition* **2000**, *6*, 121–128.
13. Berry, N.; Cheng, M.; Perkins, C. L.; Limpinsel, M.; Hemminger, J. C.; Law, M. Atmospheric-Pressure Chemical Vapor Deposition of Iron Pyrite Thin Films. *Adv. Energy Mater.* **2012**, *2*, 1124–1135.
14. Ferrer, I. J.; Sánchez, C. Characterization of FeS_2 Thin Films Prepared by Thermal Sulfidation of Flash Evaporated Iron. *J. Appl. Phys.* **1991**, *70*, 2641–2647.
15. Soukup, R. J.; Prabukanthan, P.; Ianno, N. J.; Sarkar, A.; Kamler, C. A.; Sekora, D. G. Formation of Pyrite (FeS_2) Thin Films by Thermal Sulfurization of DC Magnetron Sputtered Iron. *J. Vac. Sci. Technol. A* **2011**, *29*, 011001.
16. Pimenta, G.; Kautek, W. Thermodynamic Aspects of Pyrite Film Formation by Sulphur Conversion of Iron. *Thin Solid Films* **1992**, *219*, 37–45.
17. Smestad, G.; Ennaoui, A.; Fiechter, S.; Tributsch, H.; Hofmann, W. K.; Birkholz, M.; Kautek, W. Photoactive Thin Film Semiconducting Iron Pyrite Prepared by Sulfurization of Iron Oxides. *Solar Energy Mater.* **1990**, *20*, 149–165.
18. Morrish, R.; Silverstein, R.; Wolden, C. A. Synthesis of Stoichiometric FeS_2 Through Plasma-Assisted Sulfurization of Fe_2O_3 Nanorods. *J. Am. Chem. Soc.* **2012**, *134*, 17854–17857.
19. Wadia, C.; Wu, Y.; Gul, S.; Volkman, S. K.; Guo, J.; Alivisatos, A. P. Surfactant-Assisted Hydrothermal Synthesis of Single Phase Pyrite FeS_2 Nanocrystals. *Chem. Mater.* **2009**, *21*, 2568–2570.
20. Bi, Y.; Yuan, Y.; Exstrom, C. L.; Darveau, S. A.; Huang, J. Air Stable, Photosensitive, Phase Pure Iron Pyrite Nanocrystal Thin Films for Photovoltaic Application. *Nano Lett.* **2011**, *11*, 4953–4957.
21. Macpherson, H. A.; Stoldt, C. R. Iron Pyrite Nanocubes: Size and Shape Considerations for Photovoltaic Application. *ACS Nano* **2012**, *6*, 8940–8949.
22. Puthussery, J.; Seefeld, S.; Berry, N.; Gibbs, M.; Law, M. Colloidal Iron Pyrite (FeS_2) Nanocrystal Inks for Thin-Film Photovoltaics. *J. Am. Chem. Soc.* **2010**, *133*, 716–719.

23. Steinhagen, C.; Harvey, T. B.; Stolle, C. J.; Harris, J.; Korgel, B. A. Pyrite Nanocrystal Solar Cells: Promising, or Fool's Gold? *J. Phys. Chem. Lett.* **2012**, *3*, 2352–2356.
24. Ferrer, I. J.; Ares, J. R.; Sánchez, C. R. A Note on the Hall Mobility and Carrier Concentration in Pyrite Thin Films. *Sol. Energy Mater. Sol. Cells* **2003**, *76*, 183–188.
25. Cabán-Acevedo, M.; Faber, M. S.; Tan, Y.; Hamers, R. J.; Jin, S. Synthesis and Properties of Semiconducting Iron Pyrite (FeS_2) Nanowires. *Nano Lett.* **2012**, *12*, 1977–1982.
26. Boettcher, S. W.; Warren, E. L.; Putnam, M. C.; Santori, E. A.; Turner-Evans, D.; Kelzenberg, M. D.; Walter, M. G.; McKone, J. R.; Brunschwig, B. S.; Atwater, H. A.; *et al*. Photoelectrochemical Hydrogen Evolution Using Si Microwire Arrays. *J. Am. Chem. Soc.* **2011**, *133*, 1216–1219.
27. Tian, B.; Kempa, T. J.; Lieber, C. M. Single Nanowire Photovoltaics. *Chem. Soc. Rev.* **2009**, *38*, 16–24.
28. Kim, S.-K.; Day, R. W.; Cahoon, J. F.; Kempa, T. J.; Song, K.-D.; Park, H.-G.; Lieber, C. M. Tuning Light Absorption in Core/Shell Silicon Nanowire Photovoltaic Devices Through Morphological Design. *Nano Lett.* **2012**, *12*, 4971–4976.
29. Kelzenberg, M. D.; Boettcher, S. W.; Petykiewicz, J. A.; Turner-Evans, D. B.; Putnam, M. C.; Warren, E. L.; Spurgeon, J. M.; Briggs, R. M.; Lewis, N. S.; Atwater, H. A. Enhanced Absorption and Carrier Collection in Si Wire Arrays for Photovoltaic Applications. *Nat. Mater.* **2010**, *9*, 239–244.
30. Kelzenberg, M. D.; Turner-Evans, D. B.; Putnam, M. C.; Boettcher, S. W.; Briggs, R. M.; Baek, J. Y.; Lewis, N. S.; Atwater, H. A. High-Performance Si Microwire Photovoltaics. *Energy Environ. Sci.* **2011**, *4*, 866–871.
31. Yuan, G.; Aruda, K.; Zhou, S.; Levine, A.; Xie, J.; Wang, D. Understanding the Origin of the Low Performance of Chemically Grown Silicon Nanowires for Solar Energy Conversion. *Angew. Chem., Int. Ed.* **2011**, *50*, 2334–2338.
32. Foley, J. M.; Price, M. J.; Feldblyum, J. I.; Maldonado, S. Analysis of the Operation of Thin Nanowire Photoelectrodes for Solar Energy Conversion. *Energy Environ. Sci.* **2012**, *5*, 5203–5220.
33. Dan, Y.; Seo, K.; Takei, K.; Meza, J. H.; Javey, A.; Crozier, K. B. Dramatic Reduction of Surface Recombination by *in Situ* Surface Passivation of Silicon Nanowires. *Nano Lett.* **2011**, *11*, 2527–2532.
34. Kapadia, R.; Fan, Z.; Javey, A. Design Constraints and Guidelines for CdS/CdTe Nanopillar Based Photovoltaics. *Appl. Phys. Lett.* **2010**, *96*, 103116–3.
35. Tang, J.; Huo, Z.; Brittman, S.; Gao, H.; Yang, P. Solution-Processed Core-Shell Nanowires for Efficient Photovoltaic Cells. *Nat. Nanotechnol.* **2011**, *6*, 568–572.
36. Bierman, M. J.; Jin, S. Potential Applications of Hierarchical Branching Nanowires in Solar Energy Conversion. *Energy Environ. Sci.* **2009**, *2*, 1050–1059.
37. Bierman, M. J.; Lau, Y. K. A.; Kvit, A. V.; Schmitt, A. L.; Jin, S. Dislocation-Driven Nanowire Growth and Eshelby Twist. *Science* **2008**, *320*, 1060–1063.
38. Lau, Y. K. A.; Chernak, D. J.; Bierman, M. J.; Jin, S. Formation of PbS Nanowire Pine Trees Driven by Screw Dislocations. *J. Am. Chem. Soc.* **2009**, *131*, 16461–16471.
39. Morin, S. A.; Bierman, M. J.; Tong, J.; Jin, S. Mechanism and Kinetics of Spontaneous Nanotube Growth Driven by Screw Dislocations. *Science* **2010**, *328*, 476–480.
40. Wu, H.; Meng, F.; Li, L.; Jin, S.; Zheng, G. Dislocation-Driven CdS and CdSe Nanowire Growth. *ACS Nano* **2012**, *6*, 4461–4468.
41. de las Heras, C.; de Vidales, J. L. M.; Ferrer, I. J.; Sánchez, C. Structural and Microstructural Features of Pyrite FeS_{2-x} Thin Films Obtained by Thermal Sulfuration of Iron. *J. Mater. Res.* **1996**, *11*, 211–220.
42. Fiechter, S.; Birkholz, M.; Hartmann, A.; Dulski, P.; Giersig, M.; Tributsch, H.; Tilley, R. J. D. The Microstructure and Stoichiometry of Pyrite $FeS_{2-;x}$. *J. Mater. Res.* **1992**, *7*, 1829–1838.
43. Kleppe, A. K.; Jephcoat, A. P. High-Pressure Raman Spectroscopic Studies of FeS_2 Pyrite. *Mineral. Mag.* **2004**, *68*, 433–441.
44. Vogt, H.; Chattopadhyay, T.; Stolz, H. J. Complete First-Order Raman Spectra of the Pyrite Structure Compounds FeS_2, MnS_2 and SiP_2. *J. Phys. Chem. Solids* **1983**, *44*, 869–873.
45. Hung, A.; Muscat, J.; Yarovsky, I.; Russo, S. P. Density-Functional Theory Studies of Pyrite FeS_2(100) and (110) Surfaces. *Surf. Sci.* **2002**, *513*, 511–524.
46. de Leeuw, N. H.; Parker, S. C.; Sithole, H. M.; Ngoepe, P. E. Modeling the Surface Structure and Reactivity of Pyrite: Introducing a Potential Model for FeS_2. *J. Phys. Chem. B* **2000**, *104*, 7969–7976.
47. Murphy, R.; Strongin, D. R. Surface Reactivity of Pyrite and Related Sulfides. *Surf. Sci. Rep.* **2009**, *64*, 1–45.
48. Dodony, I.; Posfai, M.; Buseck, P. R. Structural Relationship Between Pyrite and Marcasite. *Am. Mineral.* **1996**, *81*, 6.
49. Yan, Y.; Jones, K. M.; Jiang, C. S.; Wu, X. Z.; Noufi, R.; Al-Jassim, M. M. Understanding the Defect Physics in Polycrystalline Photovoltaic Materials. *Phys. B (Amsterdam, Neth.)* **2007**, *401−402*, 25–32.
50. Zhang, H.-X.; Ge, J.-P.; Wang, J.; Wang, Z.; Yu, D.-P.; Li, Y.-D. Silica-Sheathed Pyrrotite Nanowires: Synthesis and Mechanism. *J. Phys. Chem. B* **2005**, *109*, 11585–11591.
51. Lambert, J.; Simkovich, G.; Walker, P. The Kinetics and Mechanism of the Pyrite-to-Pyrrhotite Transformation. *Metall. Mater. Trans. B* **1998**, *29*, 385–396.
52. Khanal, D. R.; Walukiewicz, W.; Grandal, J.; Calleja, E.; Wu, J. Determining Surface Fermi Level Pinning Position of InN Nanowires Using Electrolyte Gating. *Appl. Phys. Lett.* **2009**, *95*, 3.
53. Ueno, K.; Nakamura, S.; Shimotani, H.; Ohtomo, A.; Kimura, N.; Nojima, T.; Aoki, H.; Iwasa, Y.; Kawasaki, M. Electric-Field-Induced Superconductivity in an Insulator. *Nat. Mater.* **2008**, *7*, 855–858.
54. Lu, C.; Fu, Q.; Huang, S.; Liu, J. Polymer Electrolyte-Gated Carbon Nanotube Field-Effect Transistor. *Nano Lett.* **2004**, *4*, 623–627.
55. Mott, N. F. *Mott-Insulator Transition*, 2nd ed.; Taylor-Francis: London, 1990.
56. Lichtenberger, D.; Ellmer, K.; Schieck, R.; Fiechter, S.; Tributsch, H. Structural, Optical and Electrical Properties of Polycrystalline Iron Pyrite Layers Deposited by Reactive D. C. Magnetron Sputtering. *Thin Solid Films* **1994**, *246*, 6–12.
57. Ellmer, K.; Lichtenberger, D.; Ennaoui, A.; Hopfner, C.; Fiechter, S.; Tributsch, H. In *Comparison of Structural, Optical and Electrical Properties of Pyrite (FeS_2) Layers Prepared by MOCVD (Normal and Low Pressure) and Reactive Magnetron Sputtering*; Photovoltaic Specialists Conference, Conference Record of the Twenty Third IEEE, 10−14 May 1993; **1993**; pp 535−538.
58. Shklovskii, B. I.; Efros, A. L. *Electronic Properties of Doped Semiconductors*; Springer-Verlag: Berlin, 1984; pp 202−251.
59. Evans, B. J.; Johnson, R. G.; Senftle, F. E.; Cecil, C. B.; Dulong, F. The ^{57}Fe Mössbauer Parameters of Pyrite and Marcasite with Different Provenances. *Geochim. Cosmochim. Acta* **1982**, *46*, 761–775.